Influence of aerodynamic modeling on the whirl flutter stability of a propeller under axial and non-axial flow conditions

Vincent de Gaudemaris, Jean-Sébastien Schotté, Antoine Placzek, Laurent Blanc, Fabrice Thouverez

International Forum on Aeroelasticity and Structural Dynamics
IFASD 2024
17-21 June 2024, The Hague, The Netherlands

INFLUENCE OF AERODYNAMIC MODELING ON THE WHIRL FLUTTER STABILITY OF A PROPELLER UNDER AXIAL AND NON-AXIAL FLOW CONDITIONS

Vincent de Gaudemaris[1], Jean-Sébastien Schotté[1], Antoine Placzek[1], Laurent Blanc[2], Fabrice Thouverez[2]

[1]ONERA
DAAA, ONERA, Institut Polytechnique de Paris, 92320, Châtillon, France
{vincent.de_gaudemaris; jean-sebastien.schotte; antoine.placzek}@onera.fr

[2]Laboratoire de Tribologie et Dynamique des Systèmes (LTDS)
36 Av. Guy de Collongue, 69134 Ecully, France
{fabrice.thouverez; laurent.blanc}@ec-lyon.fr

Keywords: whirl flutter, aeroelasticity, low-fidelity, mid-fidelity, non-axial flow, pulse method.

Abstract: The next generation of propeller-driven aircraft raises new concerns about their stability regarding the whirl flutter phenomenon. This instability has to be evaluated early in the design phase, thereby raising a need for fast and robust prediction methods. The key to analyzing such instability is the modeling of the motion-induced aerodynamic loads on the propeller. This paper proposes to build and compare different aerodynamic modeling methods ranging from low- to mid-fidelity. The comparison of the resulting stability boundaries shows that certain low-fidelity models give results close to mid-fidelity, emphasizing the advantages of these fast low-fidelity methods for the whirl flutter prediction. The interest of mid-fidelity modeling techniques in the study of non-conventional situations is also looked at. In particular, the occurrence of whirl flutter under non-axial flow is studied. The obtained stability boundaries highlight a slight stabilizing influence, demonstrating that the axial flight situation remains a conservative framework for whirl flutter studies.

1 INTRODUCTION

In a drive to improve the efficiency of air travel, new aircraft configurations based on unconventional architectures are emerging. They favor the use of high aspect ratio wings with large diameter engines to minimize fuel consumption and maximize performance [1]. However, with the increase in wing and blade slenderness come questions about the robustness of these new configurations to the whirl flutter aeroelastic instability [1]. This phenomenon, characterized by a divergent motion of the propeller center, leads to irreversible damage and constitutes therefore an important constraint in the aircraft development process [2].

Even though it was discovered by Taylor & Browne in 1938 [3], the first concrete interests in whirl flutter date back to the 1960s after two accidents in 1959 and 1960 of the Lockheed L-188 C Electra II aircraft. Modeling of this instability requires an expression of the motion-induced aerodynamic loads on a propeller. Reed & Bland [4] used the work of Ribner [5,6], who

[1]https://aviationweek.com/shownews/paris-air-show/onera-studies-hydrogen-powered-truss-braced-wing-airliner

primarily developed the expression of the forces and moments on a propeller in pitch and yaw, to conduct the first stability analysis on a simple propeller structure. Houbolt & Reed [7] continued the investigation of this phenomenon in 1962 to create what is considered to be the reference model of whirl flutter. They developed linearized analytical expressions of the motion-induced aerodynamic loads on a rigid blade propeller by means of a quasi-steady strip theory. Rodden & Rose [8] later included them in the finite element solver *MSC Nastran* to provide a framework commonly used to this day in the aircraft certification process [2].

Since then, several efforts have been made to enhance the aerodynamic modeling of the forces and moments on the propeller. For the sake of synthesis, they can be classified from low- to mid- and even high-fidelity. The low-fidelity models rely on 2D-aerodynamic theories used in an analytical way. Usually, they start from the work of Houbolt & Reed and add improvements. Gennaretti & Greco [9] for example upgraded these expressions to consider the unsteadiness of the flow through Theodorsen's theory [10]. They conducted stability studies on a simple two degrees of freedom model and compared their results with a more advanced mid-fidelity code based on a Boundary Element Method formulation. One of the findings was that the flow modeling method could significantly alter the stability predictions. Other studies based on low-fidelity models were performed by Koch et al. [11, 12] to investigate the influence of blade flexibility through the use of an external code based on Wagner's aerodynamic theory.

Besides these low-fidelity models, mid-fidelity ones appeared to tackle complex 3D-flow effects that were incompletely modeled with 2D-aerodynamic theories. Numerous mid-fidelity studies arose mainly due to the constraint whirl flutter represented for tilt-rotors, characterized by their toggling engines positioned at the wing tip [13]. The weight of such systems combined with the increased rotor diameter made them more sensitive to whirl flutter and created a need for finer modeling from both an aerodynamic and structural standpoint. It was achieved through the use of so-called rotorcraft comprehensive codes which prevail today in the field of whirl flutter studies. They can provide modeling of the structure and of the aerodynamics on the same platform, useful for the study of complex tilt-rotor configurations [14–16] but also propeller-driven aircraft [17–19]. Other mid-fidelity studies rely on the external coupling between a structural and aerodynamic solver [20–22].

Ultimately, attempts were made to pave the way towards high-fidelity whirl flutter modeling through coupled Computational Fluid Dynamics (CFD)/Computational Structural Mechanics (CSM) simulations, especially since mid-fidelity can still present significative discrepancies with experimental results [23]. Such simulations can already be found in the field of helicopters for a non-moving rotor rotation axis [24]. However, the intrinsic precession motion of this axis during whirl flutter complicates the implementation of such coupled calculations. Verley & Dugeai [1] developed to this end a chimera approach in ONERA's CFD code to manage rigid body motion of a counter-rotating open rotor. Corle & Floros [25] went further to perform time-domain whirl flutter stability analysis with fully coupled CFD/CSM simulations. Instead of direct coupling, Reveles & Rajagopal [26] proposed a method to perform whirl flutter stability analysis by means of CFD response to imposed motion of the propeller. Despite these attempts to bridge the gap with high-fidelity analysis, this ground remains rather unexplored as it is very costly in computing time and offers less flexibility than the previously mentioned low- and mid-fidelity models.

With the desire to evaluate the influence of aerodynamic modeling on the whirl flutter stability of a rigid blade propeller, Koch et al. [27] recently compared the classical Houbolt & Reed

model with more advanced low- and mid-fidelity codes. They found that the whirl flutter stability margins could present significant discrepancies between the models and that the classical Houbolt & Reed framework could not guarantee conservatism of the results. In the spirit of this work, this paper proposes in a first part to do a review of some existing low- and mid-fidelity aerodynamic models, and details the construction of novel low-fidelity ones addressing the limitations of Houbolt & Reed's reference modeling. The methodology employed to conduct stability analysis on a simple structure model is then detailed in a second part. Finally, in a third part, the stability predictions of these models are compared for axial flow conditions before investigating with the mid-fidelity methods the unconventional and rather unstudied configuration of non-axial flow.

2 STRUCTURAL AND AERODYNAMIC MODELS

2.1 Structural model

The structural model displayed in Figure 1 is used in this study to perform stability analysis. It is the reference model for whirl flutter studies [28], and constitutes therefore a good benchmark to evaluate the influence of aerodynamic modeling. The structure is made of a rigid blade propeller rotating at constant speed Ω around a rigid pylon of length L_a. The pylon is connected to the frame by two rotational springs of stiffnesses K_ψ and K_θ, with viscous dampers of coefficient C_ψ and C_θ. The system has therefore two degrees of freedom (dof) which are the pitch θ and yaw ψ angles. These angles represent the precession motion of a nacelle on a wing, a motion inherent to whirl flutter. The whole system is immersed in a flow of speed $\vec{V}$. Two configurations are used. First, a case where the flow is along the $\vec{x}$ axis. It constitutes the reference configuration widespread in the literature as it models a propeller mounted on an airplane in axial flight [28]. Then, a more original setup is studied where the flow has components along the $\vec{x}$ and $\vec{z}$ axis. This represents a take-off or turning phase of the aircraft where the propeller is subjected to a non-negligible cross-flow. Whirl flutter studies in this last case are not numerous which leaves open questions about the influence of this cross-flow on stability.

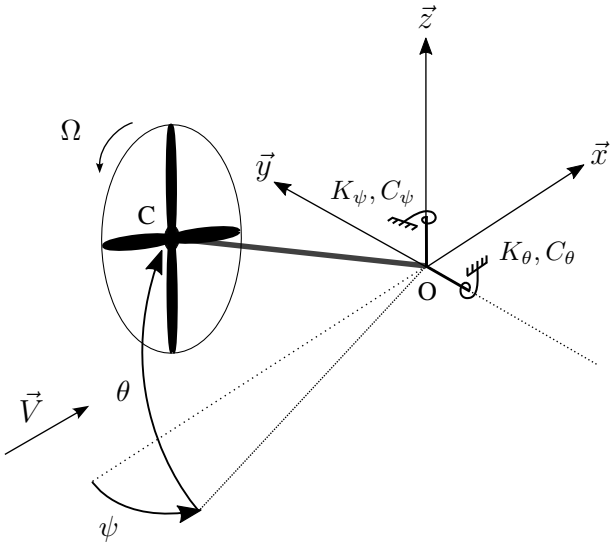

Figure 1: Classical structural model used for whirl flutter stability analysis.

Noting $\boldsymbol{u} = (\theta,\, \psi)^T$ the system's dof, the motion equation can be written as:

$$\mathbf{M_{struct}}\ddot{\boldsymbol{u}} + \mathbf{C_{struct}}\dot{\boldsymbol{u}} + \mathbf{K_{struct}}\boldsymbol{u} = \boldsymbol{m}_{aero}(\ddot{\boldsymbol{u}}, \dot{\boldsymbol{u}}, \boldsymbol{u}) \tag{1}$$

where $\mathbf{M_{struct}}$ is the mass matrix, $\mathbf{C_{struct}}$ the damping matrix and $\mathbf{K_{struct}}$ the stiffness matrix. When there are three blades or more (to avoid periodicity of the rotor's inertia in the reference

frame), the structural matrices are constant. They are expressed by:

$$\mathbf{M_{struct}} = \begin{bmatrix} J_n & 0 \\ 0 & J_n \end{bmatrix},\ \mathbf{C_{struct}} = \begin{bmatrix} C_\theta & -J_p\Omega \\ J_p\Omega & C_\psi \end{bmatrix},\ \mathbf{K_{struct}} = \begin{bmatrix} K_\theta & 0 \\ 0 & K_\psi \end{bmatrix} \tag{2}$$

with J_n the pitch and yaw inertia of the nacelle and rotor, J_p the polar inertia of the rotating parts. $\boldsymbol{m_{aero}}$ is the aerodynamic moment at the pivot point O resulting from the propeller aerodynamics loads. Its particularity is that it depends on the degrees of freedom since the induced velocities and the incidence angle of the flow on the blades evolve as the propeller center moves.

The next sections focus on obtaining an expression of the second member of the motion equation $\boldsymbol{m_{aero}}$ with different levels of fidelity. In a more general perspective of coupling with any structural model (not only the one Figure 1), the propeller forces and moments are first expressed at the propeller center C depending on the center dof in translation $\boldsymbol{u_c} = (u_c^x,\, u_c^y,\, u_c^z)^T$ and rotation $\boldsymbol{\theta_c} = (\varphi,\, \theta,\, \psi)^T$. The link with the pivot moment $\boldsymbol{m_{aero}}$ is then established in section 3 in order to perform whirl flutter stability analysis on the simple structure considered here.

2.2 Houbolt & Reed's low-fidelity aerodynamic model

Houbolt & Reed created the reference model of whirl flutter [7]. In their work, they developed an expression of the motion-induced aerodynamic loads on a rigid blade propeller under an axial flow. Starting from the expression of the elementary lift on a blade profile, they summed the forces and moments on each profile (strip theory) to obtain the resulting loads on the whole propeller. Their expression of the transverse forces ($f_c^y,\ f_c^z$) and moments ($m_c^y,\ m_c^z$) at the propeller center is written under:

$$\begin{pmatrix} f_c^y \\ f_c^z \\ m_c^y \\ m_c^z \end{pmatrix} = -\mathbf{C_a} \begin{pmatrix} \dot{u}_c^y \\ \dot{u}_c^z \\ \dot{\theta} \\ \dot{\psi} \end{pmatrix} - \mathbf{K_a} \begin{pmatrix} u_c^y \\ u_c^z \\ \theta \\ \psi \end{pmatrix} \tag{3}$$

u_c^y and u_c^z are the transverse displacements of the propeller center C whereas θ and ψ are its rotations associated to pitch and yaw motions (for the specific model displayed in Figure 1, they are linked at first order through the relations $u_c^y = -L_a\psi$ and $u_c^z = L_a\theta$). Matrices $\mathbf{C_a}$ and $\mathbf{K_a}$ represent added damping and added stiffness effects. They are expressed through:

$$\mathbf{C_a} = -\rho\pi V^2 R^3 \begin{bmatrix} -\frac{C_{y\psi}}{2RV} & -\frac{C_{y\theta}}{2RV} & \frac{C_{yq}}{2V} & -\frac{C_{yr}}{2V} \\ \frac{C_{z\psi}}{2RV} & \frac{C_{z\theta}}{2RV} & -\frac{C_{zq}}{2V} & \frac{C_{zr}}{2V} \\ -\frac{C_{m\psi}}{V} & -\frac{C_{m\theta}}{V} & \frac{C_{mq}R}{V} & -\frac{C_{mr}R}{V} \\ \frac{C_{n\psi}}{V} & \frac{C_{n\theta}}{V} & -\frac{C_{nq}R}{V} & \frac{C_{nr}R}{V} \end{bmatrix} \tag{4a}$$

$$\mathbf{K_a} = -\rho\pi V^2 R^3 \begin{bmatrix} 0 & 0 & \frac{C_{y\theta}}{2R} & -\frac{C_{y\psi}}{2R} \\ 0 & 0 & -\frac{C_{z\theta}}{2R} & \frac{C_{z\psi}}{2R} \\ 0 & 0 & C_{m\theta} & -C_{m\psi} \\ 0 & 0 & -C_{n\theta} & C_{n\psi} \end{bmatrix} \tag{4b}$$

where ρ is the air density, V the free stream velocity and R the propeller radius. The coefficients of these matrices are called the "aerodynamic derivatives". They express the dependency of the loads on the propeller motion. The derivatives linking the loads to the translation displacements

of the propeller (first two columns of $\mathbf{K_a}$) are equal to zero as these displacements are not responsible for a modification of the induced velocities nor incidence angle, resulting in no net variation of the loads. The complete analytical expression of the derivatives can be found in the paper of Rodden & Rose who synthesize Houbolt & Reed's work [8]. For example, the derivative $C_{m\psi}$ linking the change in moment m_c^y caused by a rotation in yaw ψ is expressed by:

$$C_{m\psi} = \frac{2\Omega}{V}\frac{N}{4}\frac{a_0}{2\pi}\mu\int_{\eta_0}^{1}\frac{\eta^2 c(\eta)\,F(k)}{\sqrt{\mu^2+\eta^2}}\frac{A}{\left[2+A\sqrt{1-M^2\left(1+\frac{\eta^2}{\mu^2}\right)}\right]}\,d\eta \tag{5}$$

where N is the number of propeller blades (supposed equal or greater than three to avoid time-dependency of the derivatives), a_0 is the 2D-lift coefficient curve slope (usually taken to 2π which is its value for infinitely thin profiles), c is the chord of the profile and $\mu = \frac{V}{\Omega R}$ is the advance ratio. This derivative is expressed by integration along blade span with $\eta_0 = \frac{r_0}{R}$ being the dimensionless hub radius r_0. The last coefficient of the integral is the result of the multiplication of two corrective factors:

$$C_{comp} = \frac{1}{\sqrt{1-M_r^2}} \tag{6a}$$

$$C_{3D} = \frac{A\sqrt{1-M_r^2}}{2+A\sqrt{1-M_r^2}} \tag{6b}$$

C_{comp} is the Prandtl-Glauert compressibility correction which depends on the relative Mach number M_r defined with respect to the free flow Mach number M by $M_r = M\sqrt{1+\frac{\eta^2}{\mu^2}}$. C_{3D} is a finite length correction factor used to tackle 3D flow effects such as tip vortices. It depends on the blade aspect ratio $A = \frac{R(1-\eta_0)^2}{\int_{\eta_0}^{1} c(\eta)\,d\eta}$ and comes from Prandtl Lifting Line theory applied to an elliptical wing [29]. The derivative $C_{m\psi}$ is dependent as well on a function $F(k)$ which is the real part of Theodorsen's complex lift deficiency function $C(k) = F(k) + iG(k)$. It comes from Theodorsen's theory [10] which predicts the unsteady aerodynamic loads on an oscillating profile (2D theory). The lift deficiency function models the convoluted unsteady flow effects induced by the oscillation and depends on the reduced frequency k through the relation $C(k) = \frac{H_1^{(2)}(k)}{H_1^{(2)}(k)+iH_0^{(2)}(k)}$ where $H_n^{(2)}$ is the n-th order Hankel function of the second kind. The reduced frequency is expressed as $k = \frac{\omega c}{2\sqrt{V^2+(\Omega r)^2}}$ where ω is the oscillation pulsation of the blade profiles. This pulsation is linked to the propeller vibration pulsation ω_v by two harmonics $\omega_v + \Omega$ and $\omega_v - \Omega$. For the sake of simplicity, Houbolt & Reed considered that the propeller pulsation of vibration ω_v is usually small compared to the rotor speed Ω. This choice leads to constant derivatives (independent of ω_v) which simplifies the stability problem. Please note that while the derivative $C_{m\psi}$ depends only on the real part of the lift deficiency function, some others depend on the imaginary part (e.g. $C_{y\theta}$).

There are in total 16 derivatives but due to the system symmetry, they can be reduced to 8 (for example $C_{m\psi} = -C_{n\theta}$). Note that the aerodynamic derivatives do not depend on the twist of the blades. This is due to the assumption made by Houbolt & Reed that the flow is aligned with the profile chord when the propeller is in its reference position (the twist angle of the blades is therefore implicitly defined by $\arctan\left(\frac{V}{\Omega r}\right)$). This restriction also signifies that the model cannot predict static loads (windmilling condition with no thrust or torque).

In the present paper, Houbolt & Reed's model is declined in two versions. First, a quasi-steady version where the lift deficiency function is taken equal to one which constitutes its limit when the reduced frequency tends towards zero (i.e. when the propeller is not moving). The flow is then supposed to adapt instantly to the propeller motion. Secondly, an unsteady version where the full expression of the lift deficiency function is kept (the flow unsteady effects are thus considered).

2.3 Proposed improvements in the low-fidelity aerodynamic modeling of the propeller loads

2.3.1 Restrictions of Houbolt & Reed's model

The previous Houbolt & Reed's model, despite having a reference role in whirl flutter studies, presents some limitations:

- Blade twist: it does not consider the exact evolution of the blade twist angle and thereby cannot predict static thrust. The non-utilization of the real twist angle distribution also alters the expression of the derivatives.
- Induced flow model: there is no modeling of the acceleration and rotation of the flow when it passes through the propeller. This assumption can be justified by the fact that in high-speed axial flows (where whirl flutter is more likely to occur), the induced velocities on the rotor disk are usually small compared to the free stream velocity. However, for thorough modeling of whirl flutter, induced flow models must be considered (see for example [20]).
- Unsteady aerodynamics: inclusion of unsteady aerodynamics effects through Theodorsen's lift deficiency function remains an approximate version of the complete Theodorsen theory [10]. Indeed, the rotor pulsation of vibration ω_v is neglected in the expression of the lift deficiency function $C(k)$ and additional developments derived by Theodorsen are not considered (e.g. non-circulatory flow effects).
- Airfoil simplification: the pitching moment and drag of the profiles are neglected.
- Loads components: axial force f_c^x and moment m_c^x on the propeller are not predicted. This can be explained by their non-influence on the configuration of Figure 1 but it could be of importance for systems with more than two degrees of freedom.

In an attempt to make up for these restrictions, the authors have developed in a precedent work a model declined in a quasi-steady and an unsteady formulation [30]. They are recalled herein for the sake of understanding. Note that, as for the Houbolt & Reed model, the free flow velocity is supposed to be along the $\vec{x}$ axis. A summary of all the models used in this article is given later in Table 1 but the the reader is invited to refer to it from now on for greater clarity.

2.3.2 Quasi-steady aerodynamic model

At first, an improvement of Houbolt & Reed's quasi-steady formulation is considered. This amounts to answering all limitations laid above, except the third one regarding the full Theodorsen theory which will be addressed next section.

A linearized expression of the loads regarding the propeller center translational $\boldsymbol{u_c} = (u_c^x,\, u_c^y,\, u_c^z)^T$ and rotational $\boldsymbol{\theta_c} = (\varphi,\, \theta,\, \psi)^T$ degrees of freedom is sought (the model is developed in a general way, not only for the configuration of Figure 1). Figure 2 presents a blade profile with the associated in-plane u_T and out-of-plane u_P velocities of the blade section relative to the airflow. The aerodynamic lift f_l, drag f_d and pitching moment $m_{1/4}$ are expressed at

the quarter chord point P through:

$$f_l = \frac{1}{2}\,\rho\, a_l\, c\,(u_T^2 + u_P^2)\,(\gamma - \phi - \alpha_0) \tag{7a}$$

$$f_d = \frac{1}{2}\,\rho\, c\, C_d\,(u_T^2 + u_P^2) \tag{7b}$$

$$m_{1/4} = m_0 \tag{7c}$$

where a_l is the lift coefficient curve slope, γ the blade twist angle, ϕ the inflow angle, α_0 the zero lift incidence angle, C_d the drag coefficient (supposed constant) and m_0 the static pitching moment. The angle α_0 and the constant moment m_0 are used to take into account the asymmetry of the profile as they model the non-zero lift and moment that are generated when the incidence angle $\gamma - \phi$ is zero. They can be obtained analytically depending on the profile camber (with the thin airfoil theory [29]) or can be deduced from experimental or numerical polar diagrams.

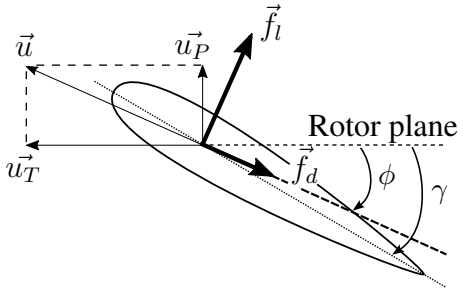

Figure 2: Lift & drag on a blade section.

The treatment of 3D flow effects is different from what is done in Houbolt & Reed's work. The averaging factor C_{3D} defined in (6) corrects all profiles in nearly the same manner ("nearly" because it depends on the relative Mach number which changes with the radius). The modeling of tip vortices therefore affects each section identically whereas in reality, it is the sections at the blade root and end that are more concerned. Moreover, Houbolt & Reed do not model the drag caused by the downwash originating from the tip vortices (induced drag). To overcome these limitations, the Prandtl lifting line theory is employed here to calculate the stationary lift and induced drag distribution along the span [29]. From these distributions, it is possible to calculate correcting factors affecting the 2D lift and drag expression (C_{3D}^l for lift and C_{3D}^d for drag). The lift coefficient curve slope and the drag coefficient are then expressed by $a_l = a_0\, C_{comp}\, C_{3D}^l$ and $C_d = C_{d_0} + C_{3D}^d$ where a_0 is the 2D-lift coefficient slope of a profile, C_{comp} the correcting factor used by Houbolt & Reed to tackle compressibility effects and C_{d_0} the 2D-drag coefficient of the profiles. a_0 and C_{d_0} can be chosen according to their ideal values ($a_0 = 2\pi$, $C_{d_0} = 0$) or can be taken from external data. It is important to keep in mind that correcting factors C_{3D}^l and C_{3D}^d are obtained regarding the stationary configuration (the propeller motion is not considered) and that certain characteristic effects of the propeller (e.g inter-blade influence, helical wake effects, etc.) are not modeled since Prandtl lifting line theory was developed for wings.

In order to obtain a linearized expression of the loads, the blade section apparent velocities are perturbed around their steady-state values – $u_T = u_T^0 + u_T'$ and $u_P = u_P^0 + u_P'$ – and (7) is linearized for small disturbed velocities (the inflow angle ϕ can be linked to the apparent velocities). These disturbed velocities u_T' and u_P' are then expressed as a function of the propeller center displacement $\boldsymbol{u_c}$ and rotation $\boldsymbol{\theta_c}$. By integrating along blade span and summing for all blades, the resulting aerodynamic force $\boldsymbol{f_c}$ and moment $\boldsymbol{m_c}$ at the propeller center can

be written in the reference frame as:

$$\begin{pmatrix} \boldsymbol{f_c} \\ \boldsymbol{m_c} \end{pmatrix} = -\mathbf{C_a} \begin{pmatrix} \dot{\boldsymbol{u}}_{\boldsymbol{c}} \\ \dot{\boldsymbol{\theta}}_{\boldsymbol{c}} \end{pmatrix} - \mathbf{K_a} \begin{pmatrix} \boldsymbol{u_c} \\ \boldsymbol{\theta_c} \end{pmatrix} + \begin{pmatrix} \boldsymbol{f_c^{stat}} \\ \boldsymbol{m_c^{stat}} \end{pmatrix} \tag{8}$$

where $\mathbf{C_a}$ is the aerodynamic damping matrix and $\mathbf{K_a}$ is the aerodynamic stiffness one. $\boldsymbol{f_c^{stat}}$ is the steady force and $\boldsymbol{m_c^{stat}}$ the steady torque at the propeller center.

To tackle induced flow effects unmodeled in the work of Houbolt & Reed, the steady-state values u_T^0 and u_P^0 are expressed taking into account the modification of the flow by the propeller that occurs when it generates thrust. Indeed, in this situation the flow is accelerated and put in rotation to satisfy the conservation of momentum. This phenomenon is modeled with the Blade Element Momentum Theory (BEMT) [31]: the stream tube passing through the propeller is discretized into rings of different radii on which balances of linear and angular momentum are performed in order to obtain the induced velocities "seen" by the blade profiles. It leads to the apparition of two corrective functions $V_a(r)$ and $V_t(r)$ in the expression of the steady state velocities $u_P^0 = \Omega r - V_t(r)$ and $u_T^0 = V + V_a(r)$. This modeling of the induced flow is therefore made at order zero as the BEMT is developed for non-moving propellers in axial flow. The consideration of the propeller motion is left out for future work as it would considerably complicate the expression of the corrective velocities.

2.3.3 Unsteady aerodynamic model

The previous quasi-steady aerodynamic model supposes that the flow, and thus the loads, instantly adapt to the movement of the blade profiles. In reality, a phase shift can appear due to wake memory effects. Theodorsen [10] developed a theory for harmonic motion to take into account this phenomenon, as well as non-circulatory effects, by introducing the lift deficiency function defined in the complex plane. Using its extension by Greenberg [32] to deal with the time dependency of the incoming velocity and the steady incidence angle, the following expression of lift and pitching moment about the $\frac{1}{4}$ chord point are obtained:

$$\begin{aligned} f_l = \pi\,\rho\,\frac{c^2}{4}\left[-\dot{u}_P\cos(\gamma) + \dot{u}_T\sin(\gamma) + \frac{c}{4}\dot{\varepsilon}\right] \\ + \frac{1}{2}\rho\,a_l\,c\,u\left[(\gamma-\phi_0-\alpha_0)u_0 + \Re\left\{C(k)\left[\widetilde{[(\gamma-\phi-\alpha_0)u]}' + \frac{c}{2}\tilde{\varepsilon}\right]\right\}\right] \end{aligned} \tag{9a}$$

$$m_{1/4} = m_0 - \pi\,\rho\,c\left(\frac{c}{4}\right)^2\left[-\dot{u}_P\cos(\gamma) + \dot{u}_T\sin(\gamma) + u_0\varepsilon + \frac{3c}{8}\dot{\varepsilon}\right] \tag{9b}$$

where $\sim$ denotes the complex expression (the physical value of a function is obtained by taking the real part $\Re\{\}$ of its complex expression[2]), ε is the angular velocity of the blade section in the rotating frame and $C(k)$ the lift deficiency function which depends on the reduced frequency $k = \frac{\omega c}{2\sqrt{{u_P^0}^2+{u_T^0}^2}}$, ω being the pulsation of u_T, u_P and ε. The notation u_0 (resp. ϕ_0) refers to the constant part of the velocity (resp. the inflow angle) and the exponent $'$ refers to the fluctuating part of the quantity $[(\gamma-\phi-\alpha_0)u]$). Drag is still given by (7b).

These expressions of the aerodynamic loads are much more complex than the ones given in last section. The quasi-steady model can be seen as an approximation of this unsteady formulation when the angular velocity ε is taken equal to zero, when the lift deficiency function is equal to

[2]For example, the complex expression of $f_0\cos(\omega t+\varphi)$ is $f_0 e^{i(\omega t+\varphi)}$

one and when the added mass terms are neglected (terms depending on $\dot{u}_T$ and $\dot{u}_P$). Houbolt & Reed's unsteady model is also a simplified version of this model. It neglects also the added mass terms and the angular velocity ε but does not take the lift deficiency function equal to one. Instead, as detailed in Section 2.2, it takes its full expression but neglects in the expression of the reduced frequency k the contribution of the rotor pulsation of vibration ω_v to the expression of ω.

When the full expressions of the force and moment are considered, a non-linear dependency on the vibratory pulsation ω_v appears due to the lift deficiency function and the loads on the whole propeller can be expressed by:

$$\begin{pmatrix} \boldsymbol{f_c} \\ \boldsymbol{m_c} \end{pmatrix} = -\mathbf{C_a}(\omega_v) \begin{pmatrix} \dot{\boldsymbol{u}}_{\boldsymbol{c}} \\ \dot{\boldsymbol{\theta}}_{\boldsymbol{c}} \end{pmatrix} - \mathbf{K_a}(\omega_v) \begin{pmatrix} \boldsymbol{u_c} \\ \boldsymbol{\theta_c} \end{pmatrix} + \begin{pmatrix} \boldsymbol{f_c^{stat}} \\ \boldsymbol{m_c^{stat}} \end{pmatrix} \tag{10}$$

As before, $\mathbf{C_a}$ is associated to damping effects and $\mathbf{K_a}$ to stiffness effects. The added mass effects appearing in (9) are included in the aerodynamic stiffness matrix since they both share the same phase.

2.4 Mid-fidelity aerodynamic models

The different models developed in sections 2.2 and 2.3 can be referred to as "low-fidelity" models. Indeed, they are mostly analytical and present some limitations regarding more advanced models. In particular:

- they rely on 2D aerodynamics theories extended in a 3D manner with the strip theory: the loads on the whole propeller are supposed to be the sum of the individual loads on each blade profile. By doing so, the influence of blade sections on each other is neglected. Corrective factors are used to model this effect but it still remains an approximate way to tackle complex 3D flow effects (flow unsteadiness, complex wake shape, etc.).
- modeling of the induced flow remains incomplete as it is done only for the stationary part since the BEMT does not consider propeller motion.
- the free flow velocity is supposed to be along the $\vec{x}$ axis, preventing stability studies in case of non-axial flow.

To tackle these limitations, this paper proposes to use more advanced models that fall within the mid-fidelity category. To this end, DUST aerodynamic solver is used [33]. This code developed by Politecnico di Milano is a flexible tool to perform unsteady aerodynamics simulation in time-domain with different levels of accuracy. A brief review of its capabilities is detailed here but the reader is invited to refer to [33] for more details. To tackle the limits of 2D-aerodynamic theories, this code considers the propeller in its entirety and does not consider anymore each blade profile independently. The wake of the propeller is unconstrained and free to evolve using a modeling mixing flat panels and vortex particles. Concerning the propeller blades, three methods are available for their modeling.

First, the Lifting Line Method (LLM) where the blades are discretized spanwise with lifting line elements. These elements rely on aerodynamic tables to compute the sectional lift, drag and moment coefficients. Despite being one-dimensional, thickness, compressibility and viscosity effects can be taken into account if they are present in the tabulated data.

Second, the Unsteady Vortex Lattice Method (UVLM) where the blades are meshed spanwise and chordwise. In this theory, thickness is not considered so the mesh is flat. Camber can

be taken into account but thickness remains unmodeled. Compressibility is itself tackled with a Prandtl-Glauert correction. A non-linear version of this model exists (NL-UVLM) where the discretization is combined with the use of aerodynamic databases (like LL elements) to introduce compressibility, thickness and viscosity corrections. However, this last version is not used in the present paper.

Finally, the Panel Method (PM) where the blade skin is meshed spanwise and chordwise but with the real shape of the blade profiles. Surface panels are used in this way on the intrados and extrados. Thickness effects can therefore be described without relying on external data. It cannot however consider viscosity effects. As for UVLM, compressibility is modeled through a Prandtl-Glauert correction factor.

DUST aerodynamic code cannot be used directly to perform eigenvalue stability analysis (see section 3) since it is a time-domain solver. Instead, it can be used to identify the frequency behavior of the aerodynamic loads on the propeller. This amounts to identifying the transfer matrix $\mathbf{H}(\omega_v)$ linking the propeller center displacement to the aerodynamic forces and moments (as a reminder, the symbol $\sim$ denotes the complex expression):

$$\begin{pmatrix} \tilde{\boldsymbol{f}}_{\boldsymbol{c}} \\ \tilde{\boldsymbol{m}}_{\boldsymbol{c}} \end{pmatrix} = \mathbf{H}(\omega_v) \begin{pmatrix} \tilde{\boldsymbol{u}}_{\boldsymbol{c}} \\ \tilde{\boldsymbol{\theta}}_{\boldsymbol{c}} \end{pmatrix} + \begin{pmatrix} \boldsymbol{f}_{\boldsymbol{c}}^{\boldsymbol{stat}} \\ \boldsymbol{m}_{\boldsymbol{c}}^{\boldsymbol{stat}} \end{pmatrix} \tag{11}$$

This matrix presents a priori a non-linear dependency on the vibratory pulsation ω_v. To identify this behavior, several harmonic excitations of the hub dof can be performed at different frequencies which, after measurement of the resulting loads, allow to track back the frequency evolution of the individual coefficients of the transfer matrix. However, this method is quite time-consuming since a lot of sinusoidal excitations have to be realized in order to have a good frequency representation of the transfer matrix. So instead of this approach, the transfer matrix is identified with pulse perturbations, in the same approach as the work of Koch et al. [11, 27]. It is performed in two steps:

- First the stationary solution is computed. Since DUST is an unsteady solver, a simulation with a sufficiently long time length is performed until proper convergence of the loads.
- Then, each dof of the hub is disturbed with a triangle perturbation (Figure 3) and the resulting propeller loads are recorded until the transient response has vanished. The resulting frequency evolution of the transfer matrix coefficients is obtained by dividing the Fourier transform of the loads with the one of the input perturbation (the stationary part of the loads identified at the first step is previously removed). For example, the coefficient H_{26} linking the disturbed transverse force on the propeller f'_y to the yaw angle ψ is given by:

$$H_{26}(\omega_v) = \frac{\mathcal{F}\left(f'_y(t)\right)}{\mathcal{F}\left(\psi(t)\right)} \tag{12}$$

  where $\mathcal{F}()$ denotes the Fourier transform. The triangle signal amplitude h is chosen so that the excitation remains sufficiently small to ward off nonlinear effects but high enough to avoid numeric noise. Regarding the triangle width Δt, a maximum value of the vibratory pulsation is estimated (depending on the practical application) and the pulse width is chosen so that its Fourier transform presents a sufficiently high magnitude up to this frequency. In practice, convergence studies must be performed (especially with regard to the time step) to ensure a proper excitation.

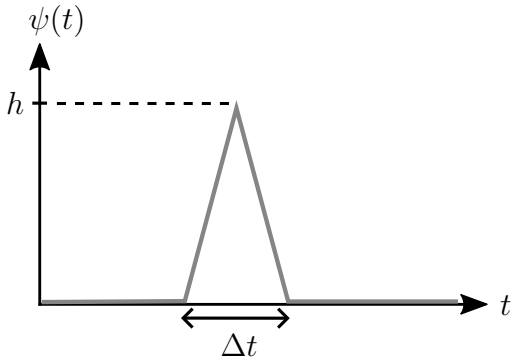

Figure 3: Example of a triangle pulse perturbation of the yaw angle ψ.

It is interesting to note that this method is not restricted to DUST code but can be employed with any aerodynamic solver. The main benefit of this approach is that it makes stability analysis possible without performing time-consuming fully coupled simulations between an aerodynamic and a structural solver, where convergence at each time step must be assured. In particular, it would be interesting in future work to use the pulse method with CFD calculations as it would allow high-fidelity whirl flutter analysis with a suitable calculation time.

Once (11) is identified, it is transformed into time domain to give:

$$\begin{pmatrix} \boldsymbol{f_c} \\ \boldsymbol{m_c} \end{pmatrix} = -\mathbf{C_a}(\omega_v) \begin{pmatrix} \dot{\boldsymbol{u}}_{\boldsymbol{c}} \\ \dot{\boldsymbol{\theta}}_{\boldsymbol{c}} \end{pmatrix} - \mathbf{K_a}(\omega_v) \begin{pmatrix} \boldsymbol{u_c} \\ \boldsymbol{\theta_c} \end{pmatrix} + \begin{pmatrix} \boldsymbol{f_c^{stat}} \\ \boldsymbol{m_c^{stat}} \end{pmatrix} \tag{13}$$

with $\mathbf{C_a}(\omega_v) = -\frac{1}{\omega_v}\Im\{\mathbf{H}(\omega_v)\}$ the aerodynamic damping matrix ($\Im$ denotes the imaginary part) and $\mathbf{K_a}(\omega_v) = -\Re\{\mathbf{H}(\omega_v)\}$ the aerodynamic stiffness matrix ($\Re$ denotes the real part). By writing the propeller center dof in the complex domain under the generic form $\begin{pmatrix} \tilde{\boldsymbol{u}}_{\boldsymbol{c}} \\ \tilde{\boldsymbol{\theta}}_{\boldsymbol{c}} \end{pmatrix} = \begin{pmatrix} \boldsymbol{u_c^0} \\ \boldsymbol{\theta_c^0} \end{pmatrix} e^{(\alpha+i\omega_v)t}$, note that the above formulation of the aerodynamic matrices is valid only when the damping factor α is zero, i.e. for neither amplified nor damped motion. However, it is not a problem for the calculation of the stability boundaries as the motion is purely sinusoidal at the flutter point.

3 STABILITY ANALYSIS METHOD

A review of the main features of the different aerodynamic models is given in Table 1. Previous sections established an expression of the force $\boldsymbol{f_c}$ and moment $\boldsymbol{m_c}$ on the propeller expressed at its center. The resulting aerodynamic moment at the pivot point of the structure Figure 1 is then expressed by:

$$\boldsymbol{m_{aero}} = \begin{pmatrix} m_c^y + L_a f_c^z + L_a f_{c_{stat}}^x \theta \\ m_c^z - L_a f_c^y + L_a f_{c_{stat}}^x \psi \end{pmatrix} \tag{14}$$

In practice, the constant part of $\boldsymbol{m_{aero}}$ is neglected since the system Figure 1 is supposed to be already in its pre-deformed shape. For the two Houbolt & Reed models and for the quasi-steady one, the motion equation (1) can then be written with (3) and (8) under:

$$\mathbf{M_{struct}}\ddot{\boldsymbol{u}} + \mathbf{C_{struct}}\dot{\boldsymbol{u}} + \mathbf{K_{struct}}\boldsymbol{u} = -\mathbf{C_{aero}}\dot{\boldsymbol{u}} - \mathbf{K_{aero}}\boldsymbol{u} \tag{15}$$

This yields in the state space domain an equation of the form $\mathbf{B}\begin{pmatrix} \dot{\boldsymbol{u}} \\ \ddot{\boldsymbol{u}} \end{pmatrix} = \mathbf{A}\begin{pmatrix} \boldsymbol{u} \\ \dot{\boldsymbol{u}} \end{pmatrix}$. The stability can then be classically estimated regarding the eigenvalues of this system: if all the eigenvalues

have a negative real part, the system is stable whereas if one has a positive real part, the system becomes unstable.

For the unsteady aerodynamic model and for the mid-fidelity ones, the motion equation is more cumbersome as a non-linear dependency of the aerodynamic matrices to the vibration pulsation exists. With (10) and (13), the motion equation (1) can be written under:

$$\mathbf{M_{struct}}\ddot{\boldsymbol{u}} + \mathbf{C_{struct}}\dot{\boldsymbol{u}} + \mathbf{K_{struct}}\boldsymbol{u} = -\mathbf{C_{aero}}(\omega_v)\dot{\boldsymbol{u}} - \mathbf{K_{aero}}(\omega_v)\boldsymbol{u} \tag{16}$$

Once in the state space domain, it yields an eigenvalue problem of the form $\mathbf{B}(\omega_v)\begin{pmatrix}\dot{\boldsymbol{u}}\\ \ddot{\boldsymbol{u}}\end{pmatrix} = \mathbf{A}(\omega_v)\begin{pmatrix}\boldsymbol{u}\\ \dot{\boldsymbol{u}}\end{pmatrix}$. This stability problem is non-linear since the vibratory pulsation ω_v constitutes the imaginary part of the sought eigenvalue. It is solved iteratively with the pk-method through a fixed-point algorithm [34] (other methods exist to make this problem linear through a rational matrix approximation of the aerodynamic loads, see for example [30]).

Table 1: Aerodynamic models summary.

	Model	Method	Blade twist	Induced flow	Stability analysis
Low-fidelity	Houbolt & Reed quasi-steady [7]	Linearized strip theory: quasi-steady lift, no pitching moment and drag	Idealized twist angle, no prevision of the static loads	No induced flow model	Linear
	Houbolt & Reed unsteady [7]	Linearized strip theory: quasi-steady lift corrected by Theodorsen's function, no pitching moment and drag	Idealized twist angle, no prevision of the static loads	No induced flow model	Linear
	Quasi-steady	Linearized strip theory: quasi-steady lift, pitching moment and drag	Real twist angle with static loads	BEMT [31]	Linear
	Unsteady	Linearized strip theory: unsteady lift and pitching moment through the complete Theodorsen theory [10] (with Greenberg's extension [32]), quasi-steady drag	Real twist angle with static loads	BEMT [31]	Non-linear
Mid-fidelity	DUST Lifting Line Method (LLM) [33]	Lifting line elements using external polar diagrams	Real twist angle with static loads	Free wake	Non-linear
	DUST Unsteady Vortex Lattice Method (UVLM) [33]	Vortex lattice elements	Real twist angle with static loads	Free wake	Non-linear
	DUST Panel Method (PM) [33]	Surface panels	Real twist angle with static loads	Free wake	Non-linear

4 NUMERICAL RESULTS

4.1 Case under study

The propeller under consideration in this paper is typically representative of twin-engine small commuter aircrafts (parameters given in Table 2). It has four blades and rotates at a constant speed. The advance ratio, defined by $\frac{V}{\Omega R}$, is a classical dimensionless number used to compare the aircraft speed to the rotor velocity. In the present study, it equals 0.8 which is classical for such kind of propellers. The blade chord evolution is represented in Figure 4. It increases up to the mid-radius and then reduces till the blade end to minimize loss caused by tip vortices. The resulting blade aspect ratio, a measure of slenderness, is 8.3.

All blade profiles are positioned so that their quarter chord points are aligned. For the low-fidelity models, 2D-drag is not considered ($C_{d_0} = 0$) and profiles are assumed to be symmetric ($m_0 = 0$ and $\alpha_0 = 0$) with a 2D-lift coefficient curve slope a_0 equals to 2π. For DUST mid-fidelity models, the same individual polar diagrams are used for the Lifting Line solver, whereas a NACA 0012 profile shape is specified for the Unsteady Vortex Lattice Method and for the Panel Method as they do not use explicit polar diagrams.

Table 2: Model parameter values.

Parameter	Symbol	Unit	Value
Number of blades	N	—	4
Rotor radius	R	m	1.2
Hub radius	r_0	m	0.15
Rotor + pylon pitch/yaw moment of inertia at the pivot point	J_n	kg.m^2	22.05
Rotor + pylon polar moment of inertia	J_p	kg.m^2	2.46
Pylon length to rotor radius ratio	$a = \frac{L_a}{R}$	—	0.7
Rotor rotation speed	Ω	rad/s	157
Wind speed	V	m/s	150
Air density	ρ	kg/m^3	1.225
Blade chord	c	m	cf Figure 4
Blade twist angle	γ	rad	cf Figure 5
Pitch/Yaw damping	C_θ / C_ψ	N.m.s/rad	0
Pitch/Yaw stiffness	K_θ / K_ψ	N.m/rad	variable

The propeller generates static thrust, which is intrinsically linked to the twist of the blades. A twist angle whose evolution with the radius r is given by $\gamma_0 = \arctan\left(\frac{V}{\Omega r}\right)$ would cause all the blade profiles to be aligned with the undisturbed inflow, thus generating almost no lift ("almost" comes from the fact that the flow is in reality disturbed by the propeller). Herein, the twist angle is chosen by $\gamma = \gamma_0 + 2.4°$. The evolution of blade twist, depicted in Figure 5, is maximum at the blade root and decreases gradually with the radius. The thrust coefficient $C_t = \frac{4\pi^2 |f_c^x|}{\rho \Omega^2 16 R^4}$ is a dimensionless number useful to measure how much the propeller is thrusting. With the present parameters, it is equal to 0.05 (measured with the low-fidelity aerodynamic models), placing this study in a case of moderate thrusting conditions.

From the standpoint of the bearing structure, the pylon length to rotor radius ratio is 0.7 which corresponds to Koch et al. "medium pylon length" situation in their article [27]. No pivot

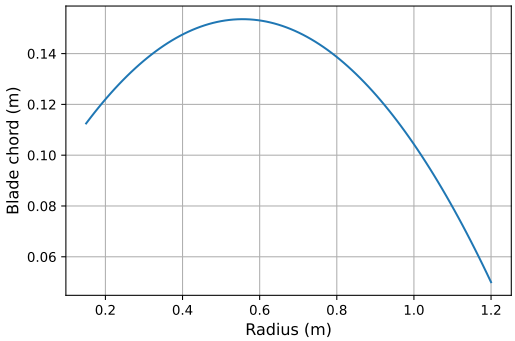

Figure 4: Chord evolution with the radius.

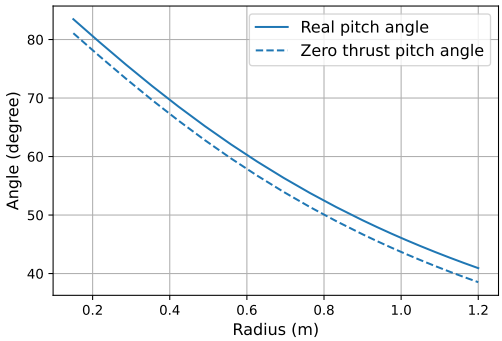

Figure 5: Twist angle distribution (the zero thrust twist angle γ_0 is plotted for comparison).

damping is considered and the mounting stiffnesses are independently varied for the parametric stability studies presented next part.

4.2 Axial flow condition

At first, the classical configuration for whirl flutter analysis is studied, i.e. when the wind is oriented along the $\vec{x}$ axis in Figure 1. The fundamental mechanisms of whirl flutter are presented in Section 4.2.1 before comparing the different aerodynamic models in Section 4.2.2.

4.2.1 Whirl flutter principle

The mounting stiffnesses play a crucial role in the whirl flutter stability of propeller engines [28]. Therefore, it is common to look at the system status depending on their values. Figure 6 consequently displays the stability boundaries for different dimensionless stiffnesses $\overline{K}_\theta = \frac{K_\theta}{J_n \Omega^2}$ and $\overline{K}_\psi = \frac{K_\psi}{J_n \Omega^2}$. These boundaries are obtained with the quasi-steady aerodynamic model presented in Section 2.3.2.

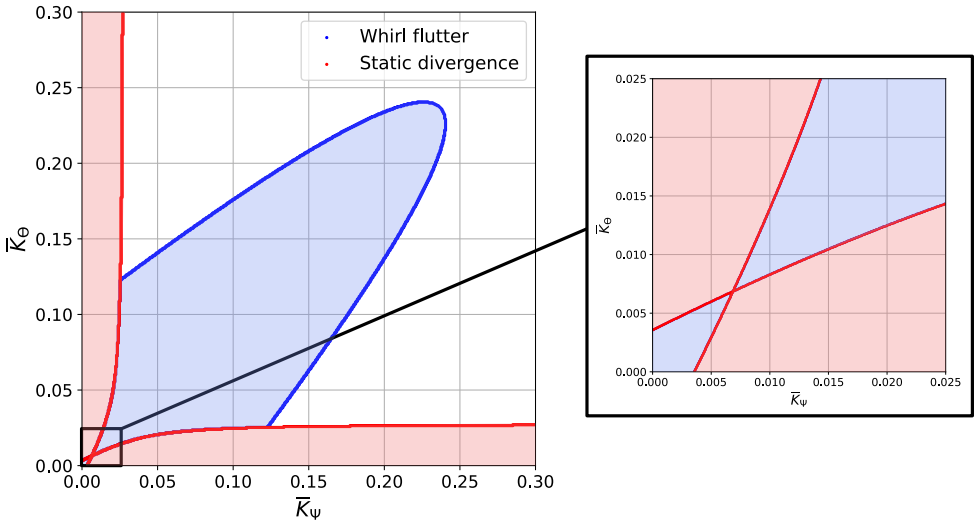

Figure 6: Stability boundaries: whirl flutter & static divergence.

Two types of instabilities are visible in this plot: a whirl flutter instability (eigenvalue with a positive real part and non-zero imaginary part) and a static divergence-like instability (eigenvalue with a positive real part and an imaginary part equal to zero). The whirl flutter instability is associated with a parabola whose vertex is located on the isotropic stiffness line ($\overline{K}_\theta = \overline{K}_\psi$). In this area, the system is subject to a divergent precession motion which occurs in a backward

whirl, i.e. in a direction opposite to the rotor rotation (for flexible propeller, it can happen in a forward whirl [28]). The two zones associated with a static divergence are parallel to the x and y axis and correspond to a situation where one of the mounting stiffnesses becomes too small to efficiently bring back the propeller aligned with the wind, causing a sudden reversal of the system. It is interesting to note that for a situation where the two stiffnesses are sufficiently small (near the origin of the identity line), the two static divergences seem to cancel each other so that the system becomes dynamically unstable. The instability then takes the form of a forward whirl, differentiating itself from the classical backward whirl instability. This situation is however rather academic since it corresponds to very low stiffness values situated very far from the stable to unstable boundary. Moreover, it does not appear in every situation as for other sets of parameters it may not happen (see for example [30]).

The effect of thrust is analyzed in Figure 7 which compares the stability boundary obtained previously (thrust coefficient $C_t = 0.05$) with the one obtained for a propeller generating no thrust (obtained by choosing the idealized twist angle γ_0). Between these two configurations, thrust has a stabilizing effect as the unstable area for the thrusting propeller is the smallest. This conclusion is also valid for other thrusting conditions since the vertex of the parabola is constantly reduced when the thrust coefficient increases (Figure 8). This stabilizing effect can be attributed to the static moment in the propeller frame that contributes to stiffness terms once passed in the fixed frame. These stiffness terms favor a forward whirl, opposite to the backward whirl occurring during whirl flutter, explaining the stabilizing influence.

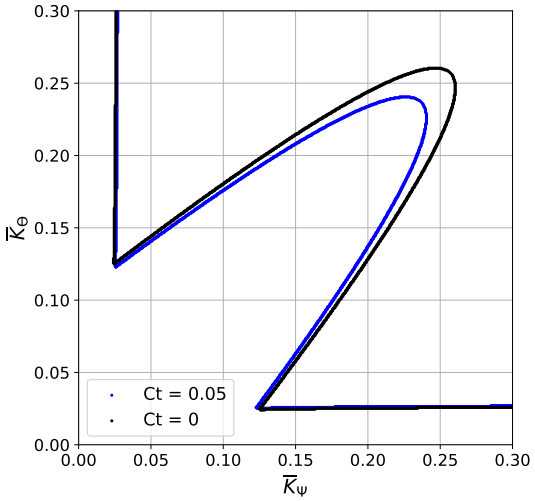

Figure 7: Thrust influence on the mounting stiffnesses stability boundary.

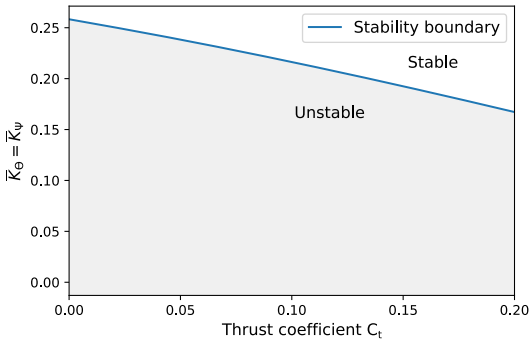

Figure 8: Evolution of the vertex of the whirl flutter boundary with the thrust coefficient.

4.2.2 Comparison of the different aerodynamic models

Now that the basic characteristics of whirl flutter have been presented, it is interesting to evaluate the influence of the different aerodynamic models on the stability boundaries. Their main features are recalled in Table 1. While the low-fidelity models give direct access to the second member matrices of the motion equation (1), the process is not as straightforward for the mid-fidelity models where they have to be built *ad hoc*. As explained in Section 2.4, it consists of two steps:

- Steady-state convergence of the propeller under axial flow.

- Pulse perturbations of the rigid body degrees of freedom to identify the aerodynamic transfer matrix.

This process is realized for the three modeling methods included in DUST being the Lifting Line Method, the Unsteady Vortex Lattice Method and the Panel Method. Following convergence studies, 200 time steps per rotor revolution and 20 spanwise discretization points are chosen. For the Unsteady Vortex Lattice Method, 10 chordwise elements are chosen whereas 14 are needed for the Panel Method to achieve proper convergence of the loads.

Steady-state

The steady flow field is represented in Figure 9 for a Panel Method simulation. Isosurfaces of the Q-criterion are displayed since it is a useful tool to represent vortex concentration. As expected, the flow is entirely symmetrical. Tip vortices are visible and propagate helically downstream. The same type of vortices are present at the blade root due to the absence of spinner. This choice, made for the sake of simplicity, is not without impact since it affects the resulting propeller loads (see for example [35] where the spinner influence on the propeller loads under non-axial flow is discussed). It should however be the subject of further investigations as it lies beyond the scope of this paper.

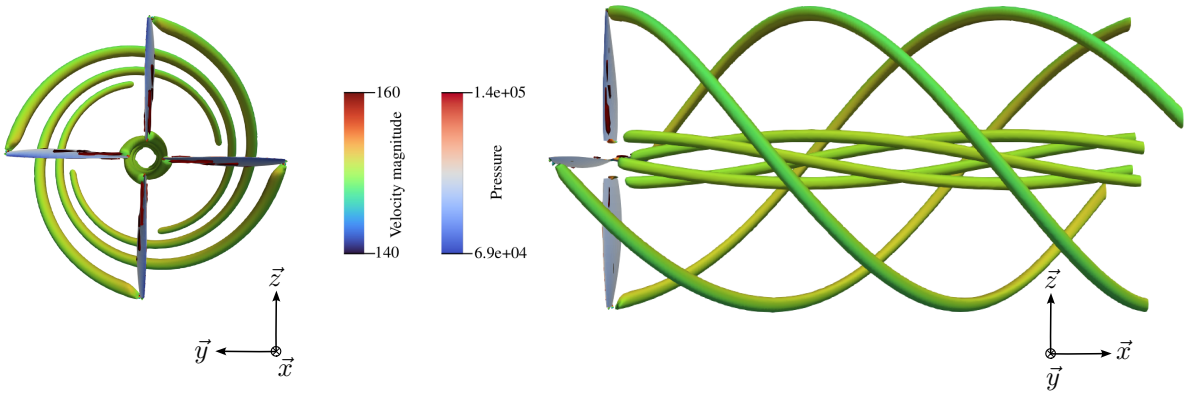

Figure 9: Front and side views of the propeller in axial flow for a DUST Panel Method simulation. Skin pressure and isosurfaces of Q-criterion (Q = 500), colored by velocity, are displayed.

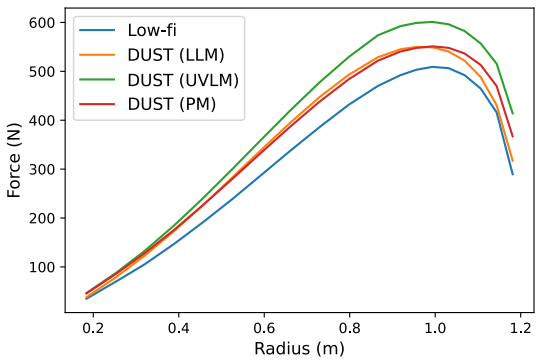

Figure 10: Comparison of the spanwise distribution of the axial force on a blade, depending on the different aerodynamic models.

Figure 10 presents a comparison of the steady axial force on a blade (along $-\vec{x}$) between the different aerodynamic models. Houbolt & Reed's results (Section 2.2) are not given since they cannot predict steady loads. Results given by the quasi-steady (Section 2.3.2) and unsteady

(Section 2.3.3) models are identical and referred to by the name "Low-fi". They are compared with all three mid-fidelity methods. For every model, the axial force increases with the spanwise position up to approximately the three-quarter radius where it suddenly drops due to tip vortices loss and blade chord reduction. As expected, differences are observed between the low-fidelity results and the mid-fidelity ones. In general, the low-fi result underestimates the loads for any radius. Differences tend to reduce at the blade root and the blade end. DUST Lifting-Line is the closest to the low-fi result. It is probably because the low-fi models employ a correction factor based on Prandtl Lifting-Line theory to tackle 3D flow effects like tip vortices. From a stationary point of view, this theory is quite close to the Lifting-Line theory used in DUST except Prandtl supposed a flat wake and does not consider the inter-blade influence while DUST does not have these limitations (it can handle any wake shape such as the helical one observed here). Disparities are also observed between the mid-fidelity results since the Unsteady Vortex Lattice Method overestimates the force regarding the other two methods. The profile thickness influence (comparison between UVLM and PM) seems therefore to lower the loads. Results given by the Lifting Line Method and Panel Method are however quite close except at the blade end where discrepancies appear.

Identification of the mid-fidelity aerodynamic transfer matrices

Once the steady state is computed for all three DUST modeling methods, pulse perturbations of the propeller rigid body modes are prescribed to determine the aerodynamic transfer matrix. Due to the system symmetry, only two perturbations are needed for the stability analysis (one perturbation in pitch or yaw and one perturbation of the transverse displacement along the $\vec{y}$ or $\vec{z}$ axis). Coefficients of the aerodynamic transfer matrix are then obtained by dividing the Fourier transform of the individual load components with the Fourier transform of the imposed pulse motion (in this case a triangle signal), see (12). Figure 11 illustrates the procedure by showcasing with DUST Lifting Line Method the evolution of the H_{22} coefficient linking the force along the $\vec{y}$ axis to the propeller displacement along the same axis u_c^y. Three simulations with an imposed sinusoidal motion at pulsations $\{$20-60-100$\}$rad/s were also performed to validate the results given by the pulse method. Both cases coincide which validates this procedure. This method is advantageous since only one simulation gives access to the coefficient frequency dependency whereas otherwise, multiple simulations with imposed sinusoidal motion (at different frequencies) should be performed to obtain the coefficient value on the frequency band of interest.

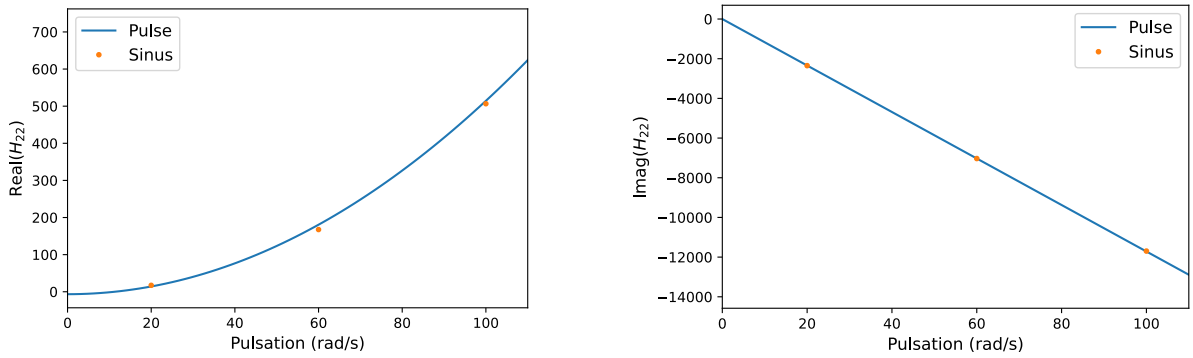

Figure 11: Real (left) and imaginary (right) parts of the H_{22} coefficient of the transfer matrix obtained with a pulse excitation (DUST Lifting Line solver). Results acquired with a harmonic excitation are also displayed for validation.

A constant real part and a linear imaginary part of the coefficients of matrix $\mathbf{H}$ would produce

constant stiffness and damping matrices. Even though the second condition is verified here for H_{22}, its real part is not constant which prevents the use of such constant matrices that could render the stability problem linear. Instead, the true evolution of these matrices is kept and the stability problem is solved non-linearly with (16).

Stability analysis

The aerodynamic transfer matrix being identified for all three mid-fidelity aerodynamic models, it is now possible to conduct stability analysis and to compare these predictions with the ones given by low-fidelity models. Figure 12 displays the boundaries, regarding the mounting stiffnesses, obtained with these different models (the low-fidelity models have dotted or dashed boundaries while the mid-fidelity models have plain ones). First, it is observed that the static divergence boundaries coincide between all models. On these frontiers, the system does not move since the associated pulsation of the unstable mode is zero. Therefore, such similarities can be explained by the weak influence of the flow's unsteady effects on these boundaries, especially since they are at the origin of the model differences. The whirl flutter boundaries and especially the position of the vertex are rather diverse between the different aerodynamic theories. The mid-fidelity results seem quite grouped and positioned between the two low-fi unsteady and the two low-fi quasi-steady models. The two low-fidelity quasi-steady models constitute a conservative framework as they overestimate the stability boundaries given by the mid-fidelity models. However, they are less precise than their unsteady counterparts which better approach the mid-fidelity results but are in turn non-conservative since they underestimate the vertex position. It is interesting to note that the quasi-steady (resp. unsteady) model developed by the authors better approaches mid-fi results than Houbolt & Reed's quasi-steady (resp. unsteady) one. Thus, the consideration of the real twist angle distribution with a modeling of the induced flow and the use of the full terms of Greenberg's theory constitutes a good improvement of the reference models. Regarding the mid-fidelity results, it is interesting to note that the Lifting Line boundary is nearly identical to the one obtained with the Panel Method. The Unsteady Vortex Lattice Method for its part leads to a reduced unstable area compared to these last two methods.

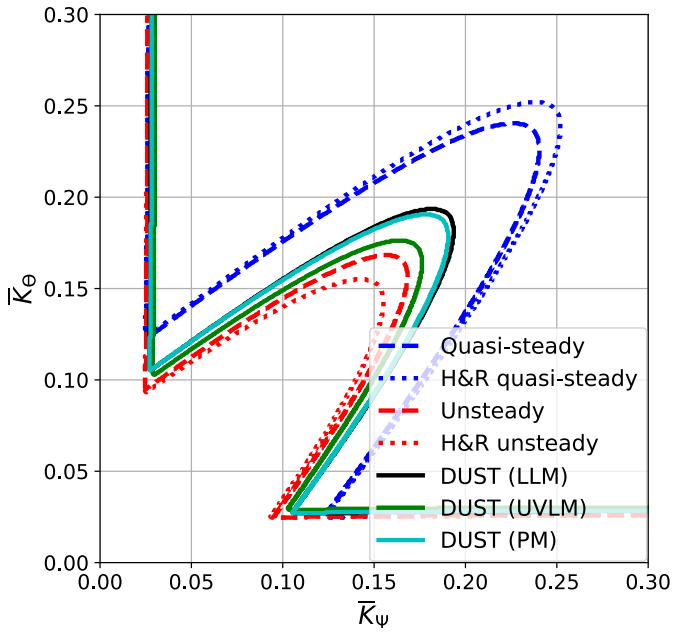

Figure 12: Stability boundaries comparison between different aerodynamic models.

As noticed by Koch et al. [27], these conclusions may vary for different sets of parameters, especially regarding the pylon length to rotor radius ratio a. Readers are therefore invited to refer to the above-mentioned work for further details regarding the influence of mid-fidelity modeling techniques on the stability boundaries.

An interesting behavior was noticed in [30] when a vertical translation of the system is free to happen through the addition of a vertical spring of stiffness K_z at the pivot point O. With the quasi-steady and unsteady aerodynamic models, unconventional stability graphs were obtained with the presence of islands of instability. This unfamiliar behavior is also obtained here with the mid-fidelity models when the rotor mass m is reduced by a factor 10, with a pylon length to rotor radius ratio of 0.1 and with a dimensionless vertical pulsation $\sqrt{\frac{K_z}{m\Omega^2}}$ of 0.69. The resulting stability map obtained with DUST Lifting Line Method (with and without vertical motion of the pivot point) and with the low-fidelity unsteady model (with vertical motion) is displayed in Figure 13. It is interesting to note that the vertical spring stabilizes overall the system as the unstable areas obtained with the vertical translation are located inside the area of instability obtained with a fixed pivot point. When a vertical translation is possible, an unstable area is detached from the rest of the unstable zone. As explained in [30], this phenomenon is caused by the vertical spring-mass system that plays the role of a tuned mass damper, concentrating and dissipating aerodynamically the vibratory energy of the system. It occurs mainly when its characteristic frequency matches the whirl frequency which in the case of Figure 13 corresponds to the peninsular area separating the island of instability from the rest of the unstable zone. At this point, the vertical motion induced by the translational spring extracts enough energy to make the system locally stable, thus isolating an island of instability.

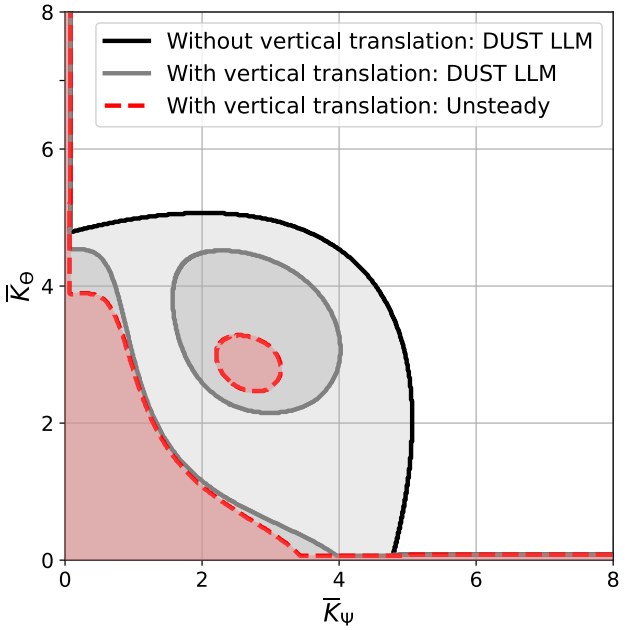

Figure 13: Stability boundaries with and without vertical motion of the pivot point.

4.3 Non-axial flow condition

Whirl flutter studies carried out in the previous section add on the classical studies available in the literature for axial flow conditions. The case of non-axial flow, representing for example a climbing or turning phase of the aircraft, is subject however to far fewer studies. Reed [36]

briefly examined the influence of flow angle using experimental propeller derivatives. He found a stabilizing influence of this angle on the instability boundaries. The same stabilizing influence was noticed by Kunz [13] who analyzed this configuration with a quasi-steady aerodynamic model taking into account an angle of the nacelle with respect to the free stream velocity. However, these two studies were devoted to a state-of-the-art on whirl flutter modeling and therefore addressed only shortly this subject. The relative absence of this topic in literature can be explained by the complex phenomena arising when modeling such configuration which limits the use of low-fidelity aerodynamic models (classical Houbolt & Reed's derivatives as well as the low-fidelity models developed by the authors do not consider non-axial flow). Indeed, the peculiarity of this configuration lies in the variation of the flow incidence angle with the azimuthal position of the blade. Figure 15 presents its evolution, at three-quarters of the propeller radius, for a flow angle of 10° (Figure 14). For an axial wind, the profile incidence angle remains constant regardless of the azimuthal position of the blade. In the present situation, it changes significantly covering values from nearly $-10°$ to $+10°$. The angle is the greatest for a descending blade ($90°$ position) when the cross-flow is frontal and adds to the flow induced by the blade rotation. On the other hand, the angle is the smallest when the blade is ascending ($270°$ position) since the cross-flow is then coming from its back and deduces from the flow induced by the rotation. This situation generates periodic loads on the blade at the rotor frequency (so-called 1P loads for one per revolution). These loads can reach substantial amplitude and therefore generate significant blade vibrations. Even though this study concerns rigid blade propellers, it would be interesting in future works to take into account blade flexibility in the study of such phenomenon.

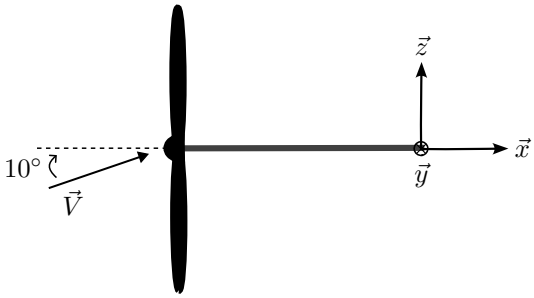

Figure 14: 10° flow angle.

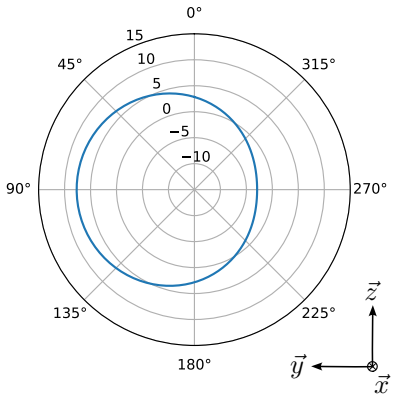

Figure 15: Incidence angle at three-quarters of the propeller radius as a function of the blade azimuthal position (front view of the propeller).

Due to the high values covered by the blade incidence angle, nonlinear polar diagrams are used to account for the lift loss due to stall at high angles of incidence (Figure 16). To tackle compressibility effects, these polar diagrams are Mach dependent (at blade tip, it reaches 0.7). It results in a slight increase of the lift coefficient curve slope when the Mach grows.

It is found that the static propeller force $\boldsymbol{f_c^{stat}}$ and moment $\boldsymbol{m_c^{stat}}$ are slightly periodic with a frequency equal to four times the rotation speed (four being the number of blades). However, the amplitude of oscillation is very small which means the 1P loads of each blade seem to compensate each other so that the resulting loads on the whole propeller are almost constant. This phenomenon is visible in Figure 17 where the time evolution of the axial force on a single blade and on the whole propeller are displayed. Since the propeller loads are nearly constant,

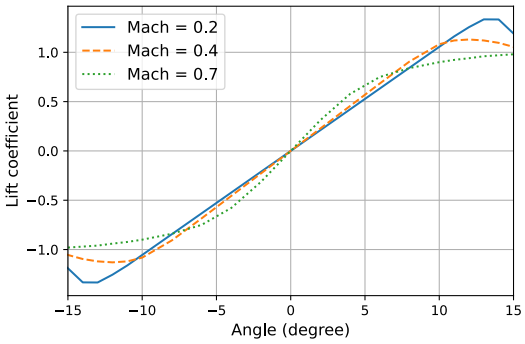

Figure 16: Blade section lift coefficient polar diagram for different Mach numbers.

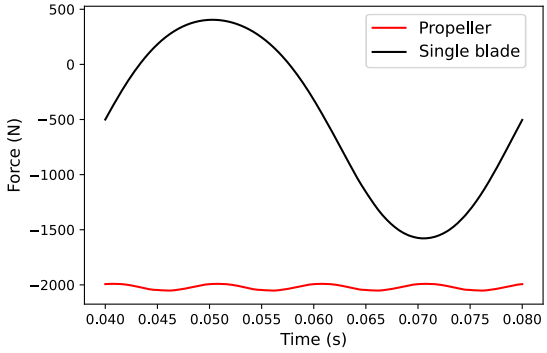

Figure 17: Comparison of the axial force on one blade and on the whole propeller (DUST Lifting Line Method simulation).

the system is supposed to be time-independent and the pulse method can be employed to determine the aerodynamic transfer matrix $\mathbf{H}(\omega_v)$. The time-independency is necessary as the pulse method cannot capture the time-evolution of the coefficients of $\mathbf{H}(\omega_v)$. Otherwise, it would require tools to analyze the stability of systems with periodic coefficients, such as Floquet analysis [37]. Also, note that static forces $\boldsymbol{f_c^{stat}}$ and moments $\boldsymbol{m_c^{stat}}$ have now components along the three axes compared to the axial flow case where they were only existing along the $\vec{x}$ axis.

The steady flow field is displayed in Figure 18. For a propeller in axial wind, the flow was entirely symmetric and the isosurfaces of Q-criterion were perfectly helical (cf Figure 9). However, strong dissymmetries are present here due to the cross-flow. As for the incidence angle, the blades going down create more vorticity than the blades going up. It prevents the isosurfaces from wrapping finely around the rotation axis. The vertical component of the flow also generates a slightly upward-directed wake.

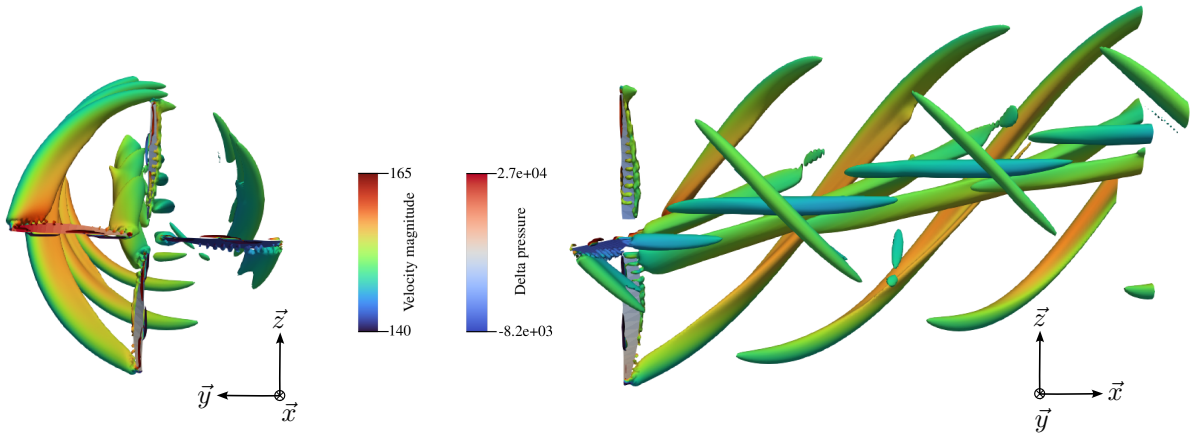

Figure 18: Front and side views of the propeller under a 10-degree flow angle for a DUST Lifting Line simulation. Skin delta pressure and isosurfaces of Q-criterion (Q = 500), colored by velocity, are displayed.

To obtain the aerodynamic transfer matrix, pulse perturbations are realized on the $\vec{y}$ and $\vec{z}$ translation and rotation of the propeller center (the $\vec{x}$ component does not intervene for the structure Figure 1 and is therefore left out). While the symmetry of a propeller in axial wind made it possible to perform only two perturbations, all four perturbations have to be realized here. It is important to keep in mind that this process wipes out the system 4Ω periodicity since the

identified transfer matrix is time-independent (but depends on the frequency). As mentioned previously, given that the periodicity is very weak, it should not be of primary importance.

The resulting stability graph is presented in Figure 19. One main difference with respect to the case of axial flow is that the graph is now asymmetric regarding the identity line. It leans to the side of the x-axis as the system is now more stable in pitch than in yaw. Moreover, the system's overall stability is increased as the position of the vertex is reduced (this stabilizing influence was also noticed by Reed [36] and Kunz [13]). These two effects are in fact caused by the non-linearity of the polar diagrams. Indeed, the same graph obtained with linear diagrams (as in Section 4.2.2) presents almost identical boundaries between the axial and non-axial flow conditions. The dissymmetry can be explained by the difference between the equivalent pitch and yaw aerodynamic stiffness at the pivot point. Indeed, for a displacement θ, the resulting aerodynamic moment at the pivot point along the $\vec{y}$ axis is lesser than the moment along the $\vec{z}$ axis for a motion ψ of the same magnitude. This difference is caused by the lift-loss effects at high angles of incidence (visible in Figure 16) that are stronger due to the vertical flow component for a motion in pitch than in yaw. These lift-loss effects are also responsible for the system's overall stabilization as it reduces the magnitude of the derivative $C_{n\theta}$ compared to $C_{m\psi}$ (whereas they are of equal magnitude for the case with axial wind).

From a general standpoint, the stability boundaries for the case with non-axial flow are almost entirely inside the unstable area obtained with an axial wind. This should be verified for other configurations but is interesting since it grants the axial flight setup a conservative status, useful as this latter case is simpler to study (with low-fidelity models for example).

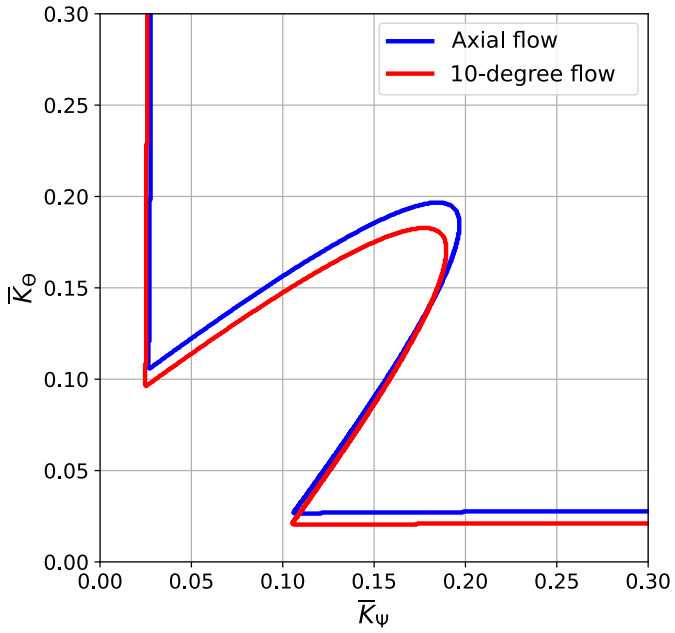

Figure 19: Stability graph with an axial vs non-axial flow (DUST Lifting Line Method simulation).

5 CONCLUSION

The first aim of this paper was to develop aerodynamic models, ranging from low- to mid-fidelity, in order to compare and analyze their predictions of the whirl flutter stability of a simple structure. Starting from the classical well-known low-fidelity model of Houbolt & Reed, two new models (quasi-steady and unsteady) previously developed by the authors were used in an attempt to address the limitations of the reference modeling. With a view of having more realistic results, DUST aerodynamic solver was employed, in conjunction with the pulse method, to create three different mid-fidelity models (based respectively on the Lifting Line Method, the Unsteady Vortex Lattice Method and the Panel Method). All these models were utilized to study the stability of a simple propeller-airplane structure immersed in an axial flow. The mid-fidelity models gave rather clustered results, positioned between the unsteady and the quasi-steady version of the low-fidelity models. The low-fidelity model giving the best results is the unsteady version developed by the authors, thus highlighting the importance of extending the hypothesis of Houbolt & Reed's modeling.

Stability studies were also performed in the case of non-axial flow, representative of take-off or turning phase of the aircraft. Such situation, little studied in the literature, goes beyond the limits of the low-fidelity models and constitutes a good example of the utility and versatility of the mid-fidelity ones. Results demonstrated a stabilizing influence of the cross-flow, although the stability boundaries were only slightly modified. This therefore makes the axial flow set up a conservative case for whirl flutter studies, even though this should be verified for other sets of parameters.

The structural model used in this paper is rather simple and an extension of this study to more complex structures, including blade deformation, should be addressed. In particular, an external coupling of the different aerodynamic models with a finite element solver will be implemented to analyze the stability of a full wing-nacelle-propeller system. Also, the influence of the wing aerodynamics and its interference with the propeller should be studied, especially with the mid-fidelity aerodynamic models that can easily tackle such complex situations. Finally, it would be interesting to compare the presented results with stability studies coming from CFD calculations (obtained with the pulse method). This would provide whirl flutter comparison across the entire fidelity spectrum, useful to benchmark the different models.

ACKNOWLEDGEMENT

This project has received funding from the Clean Sky 2 Joint Undertaking (JU) under grant agreement number 945583 within the frame of the ADEC project, and from the French Civil Aviation Authority under the France 2030 investment plan. The JU receives support from the European Union's Horizon 2020 research and innovation program and the Clean Sky 2 JU members other than the Union. The results, opinions, conclusions, etc., presented in this work are those of the authors only.

6 REFERENCES

[1] Verley, S. and Dugeai, A. (2015). Installed counter-rotating open rotor whirl flutter phenomenon investigations using elsA solver. In *International Forum on Aeroelasticity and Structural Dynamics (IFASD), Saint Petersburg, Russia*.

[2] Čečrdle, J. (2015). *Whirl Flutter of Turboprop Aircraft Structures*. Elsevier.

[3] Taylor, E. S. and Browne, K. A. (1938). Vibration isolation of aircraft power plants. *Journal of the Aeronautical Sciences*, 6(2), 43–49.

[4] Reed, W. H. and Bland, S. R. (1961). An analytical treatment of aircraft propeller precession instability. Tech. Rep. D-659, NACA.

[5] Ribner, H. S. (1945). Formulas for propellers in yaw and charts of the side-force derivative. Tech. Rep. 819, NACA.

[6] Ribner, H. S. (1945). Propellers in yaw. Tech. Rep. 820, NACA.

[7] Houbolt, J. C. and Reed, W. H. (1962). Propeller-nacelle whirl flutter. *Journal of the Aerospace Sciences*, 29(3), 333–346.

[8] Rodden, W. and Rose, T. (1989). Propeller/nacelle whirl flutter addition to MSC/Nastran. In *1989 MSC World User's Conference*.

[9] Gennaretti, M. and Greco, L. (2008). Whirl flutter analysis of prop-rotors using unsteady aerodynamics reduced-order models. *The Aeronautical Journal*, 112(1131), 261–270.

[10] Theodorsen, T. (1935). General theory of aerodynamic instability and the mechanism of flutter. Tech. Rep. 496, NACA.

[11] Koch, C. (2022). Whirl flutter stability assessment using rotor transfer matrices. In *International Forum on Aeroelasticity and Structural Dynamics (IFASD), Madrid, Spain*.

[12] Koch, C. and Koert, B. (2023). Including blade elasticity into frequency-domain propeller whirl flutter analysis. *Journal of Aircraft*, Article in Advance.

[13] Kunz, D. L. (2005). Analysis of proprotor whirl flutter: review and update. *Journal of Aircraft*, 42(1).

[14] Shen, J. and Kang, H. (2017). Comparison study of tiltrotor whirl flutter using two rotorcraft comprehensive analyses. *Journal of Aircraft*, 54(2).

[15] Yeo, H., Bosworth, J., Acree, C. W., et al. (2018). Comparison of CAMRAD II and RCAS predictions of tiltrotor aeroelastic stability. *Journal of the American Helicopter Society*, 63(2).

[16] Cocco, A., Mazzetti, S., Masarati, P., et al. (2022). Numerical whirl–flutter analysis of a tiltrotor semi-span wind tunnel model. *CEAS Aeronautical Journal*, 13, 923–938.

[17] Acree, C. W. and Hoffman, K. (2004). Whirl flutter studies for a SSTOL transport demonstrator. In *Proceedings of the AHS 4th Decennial Specialist's Conference on Aeromechanics*. San Francisco, USA.

[18] Hoover, C. B. and Shen, J. (2018). Parametric study of propeller whirl flutter stability with full-span model of X-57 Maxwell aircraft. *Journal of Aircraft*, 55(6).

[19] Hoover, C. B. and Shen, J. (2019). Fundamental understanding of propeller whirl flutter with multibody dynamics analysis. In *Proceedings of the AIAA Scitech 2019 Forum*. San Diego, USA.

[20] Corle, E., Floros, M., and Schmitz, S. (2021). On the influence of inflow model selection for time-domain tiltrotor aeroelastic analysis. *Journal of the American Helicopter Society*, 66(3).

[21] Cocco, A. and Savino, A. (2024). Tiltrotor whirl-flutter assessment by multifidelity aerodynamic models. In *Proceedings of the AIAA SCITECH 2024 Forum*. Orlando, USA.

[22] Böhnisch, N. and Braun, C. (2024). About the wing and whirl flutter of a slender wing–propeller system. *Journal of Aircraft*, Article in advance.

[23] Kreshock, A., Thornburgh, R. P., and Yeo, H. (2019). Comparison of comprehensive analyses predicting whirl flutter stability of the Wing and Rotor Aeroelastic Test System. *Journal of the American Helicopter Society*, 64(4).

[24] Yeo, H., Potsdam, M., and Ormiston, A. (2011). Rotor aeroelastic stability analysis using coupled Computational Fluid Dynamics/Computational Structural Dynamics. *Journal of the American Helicopter Society*, 56(4).

[25] Corle, E. and Floros, M. (2019). Transient CFD/CSD tiltrotor stability analysis. In *AIAA SCITECH 2019 Forum*. San Diego, USA.

[26] Reveles, N. and Rajagopal, A. (2024). Application of a novel stability method to CFD based whirl flutter analysis. In *AIAA SCITECH 2024 Forum*. Orlando, USA.

[27] Koch, C., Böhnisch, N., Verdonck, H., et al. (2024). Comparison of unsteady low- and mid-fidelity propeller aerodynamic methods for whirl flutter applications. *Applied Sciences*, 14(2:850).

[28] Reed, W. H. (1966). Propeller-rotor whirl flutter: A state-of-the-art review. *Journal of Sound and Vibration*, 4(3), 526–444.

[29] Katz, J. and Plotkin, A. (2001). *Low-Speed Aerodynamics*. Cambridge University Press, 2nd ed.

[30] de Gaudemaris, V., Schotté, J.-S., Placzek, A., et al. (2023). Unsteady aerodynamic modeling of whirl flutter on a bending wing. In *Proceedings of EURODYN 2023: XII International Conference on Structural Dynamics*. Delft, The Netherlands.

[31] Burton, T., Jenkins, N., Sharpe, D., et al. (2011). *Wind Energy Handbook*. John Wiley and Sons.

[32] Greenberg, J. M. (1947). Airfoil in sinusoidal motion in a pulsating stream. Tech. Rep. 1326, NACA.

[33] Tugnoli, M., Montagnani, D., Syal, M., et al. (2021). Mid-fidelity approach to aerodynamic simulations of unconventional VTOL aircraft configurations. *Aerospace Science and Technology*, 115.

[34] Hassig, H. J. (1971). An approximate true damping solution of the flutter equation by determinant iteration. *Journal of Aircraft*, 8(11), 885–889.

[35] Ortun, B., Boisard, R., and Gonzalez-Martino, I. (2012). Assessment of propeller 1P loads predictions. *International Journal of Engineering Systems Modelling and Simulation*, 4(1-2).

[36] Reed, W. H. and Bennett, R. M. (1963). Propeller whirl flutter considerations for V/STOL aircraft. In *Cal/Trecom Symposium Proceedings volume III. Dynamic Load Problems Associated with Helicopters and V/STOL Aircraft.*

[37] Johnson, W. (2013). *Rotorcraft Aeromechanics*. Cambridge University Press.

COPYRIGHT STATEMENT